Phase Engineering of 2D Tin Sulfides

*Zafer Mutlu, Ryan J. Wu, Darshana Wickramaratne, Sina Shahrezaei, Chueh Liu, Selcuk Temiz, Andrew Patalano, Mihrimah Ozkan, Roger K. Lake, K. A. Mkhoyan, and Cengiz S. Ozkan**

Tin sulfides can exist in a variety of phases and polytypes due to the different oxidation states of Sn. A subset of these phases and polytypes take the form of layered 2D structures that give rise to a wide host of electronic and optical properties. Hence, achieving control over the phase, polytype, and thickness of tin sulfides is necessary to utilize this wide range of properties exhibited by the compound. This study reports on phase-selective growth of both hexagonal tin (IV) sulfide SnS_2 and orthorhombic tin (II) sulfide SnS crystals with diameters of over tens of microns on SiO_2 substrates through atmospheric pressure vapor-phase method in a conventional horizontal quartz tube furnace with SnO_2 and S powders as the source materials. Detailed characterization of each phase of tin sulfide crystals is performed using various microscopy and spectroscopy methods, and the results are corroborated by ab initio density functional theory calculations.

1. Introduction

Two-dimensional (2D) tin sulfides belong to a broad class of van-der-Waal (vdW) materials that have been the subject of intense research. Their constituent elements tin (Sn) and sulfur (S) are inexpensive and abundant in nature. The atomically thin geometry combined with the ability to tune the electronic structure of 2D tin sulfides as a function of thickness makes them attractive candidates to be used in nanoelectronics and optoelectronic devices.[1] These sulfides can crystallize in a variety of crystal phases, such as tin disulfide (SnS_2) and tin monosulfide (SnS), which possess distinct physical and electronic properties.[2] Therefore, identifying approaches for controlling crystal phase is essential for tailoring the properties of these materials to specific applications.

Tin sulfides possess desirable properties for numerous electronic and optical applications. SnS_2 is an intrinsic n-type layered semiconductor with a bandgap of 2.18–2.44 eV.[3–6]

Z. Mutlu, S. Shahrezaei, C. Liu, S. Temiz
Materials Science and Engineering Program
University of California
Riverside, CA 92525, USA

R. J. Wu, Prof. K. A. Mkhoyan
Department of Chemical Engineering
and Materials Science
University of Minnesota
Minneapolis, MN 55455, USA

Dr. D. Wickramaratne,[+] Prof. M. Ozkan, Prof. R. K. Lake
Department of Electrical and Computer Engineering
University of California
Riverside, CA 92525, USA

DOI: 10.1002/smll.201600559

A. Patalano
Department of Chemistry
University of California
Riverside, CA 92525, USA

Prof. C. S. Ozkan
Department of Mechanical Engineering
University of California
Riverside, CA 92525, USA
E-mail: cozkan@engr.ucr.edu

[+]Present address: Materials Department, University of California, Santa Barbara, CA 93106, USA

© 2016 Wiley-VCH Verlag GmbH & Co. KGaA, Weinheim

Potential applications of SnS_2 include novel electronics devices, flexible electronics, optoelectronics, and energy storage.[7–10] The high electron affinity of SnS_2 makes it a suitable candidate to achieve broken-gap heterostructures which enable the design and operation of 2D tunnel field-effect transistor (TFETs).[7,11] Moreover, SnS_2 crystals show high charge carrier mobility (≈230 cm^2 $(Vs)^{-1}$) combined with high on/off current ratios (>10^6) in field-effect transistors (FETs), fast photocurrent response time (≈5 µs) in photodetectors, and high theoretical specific capacity (≈920 $mAhg^{-1}$) in lithium-ion batteries (LIBs) as the anode material.[1,9,12] On the other hand, SnS is an intrinsically p-type layered semiconductor with an indirect and a direct bandgap at ≈1–1.1 and ≈1.3–1.5 eV, respectively.[3,13–16] The desirable bandgap, high absorption coefficient (>10^4 cm^{-1}) and sensitivity of its properties to changes in dimensionality, and elemental composition make SnS a promising material for optoelectronic applications.[15,17–21] Furthermore, combined SnS and SnS_2 heterostructures have been reported to show improved photocatalytic performance on photodegrading organic dyes, compared with that of as-synthesized pure phases of SnS and SnS_2.[4]

Selective pure phase synthesis of single crystalline tin sulfides is a challenging task due to the high sensitivity of the different phases to growth conditions. Tin sulfides have been previously synthesized mostly in the form of bulk single crystals or thin films. The bulk single crystals have been grown by the Bridgman method[22,23] and chemical vapor transport;[2,24] the thin films have been synthesized using various deposition methods.[5,25–27] However, relatively few studies have reported the synthesis of 2D crystals of SnS_2[3,9,28] and SnS[3,29] using vapor-phase methods.

In this study, we demonstrate phase-controlled synthesis of 2D SnS_2 and SnS crystals using an atmospheric pressure vapor-phase method. The fundamental structural and electronic properties of each crystal phase are comprehensively investigated using optical microscopy, atomic force microscopy (AFM), scanning electron microscopy (SEM), scanning transmission electron microscopy (STEM), Raman spectroscopy, and ultraviolet photoelectron spectroscopy (UPS) and compared with results of ab initio density functional theory (DFT) calculations.

2. Results and Discussion

2.1. Morphology and Atomic Structure

2D tin sulfide crystals with lateral sizes over tens of microns were synthesized by atmospheric pressure vapor-phase growth method in a horizontal quartz tube furnace as shown in **Figure 1**a. In a typical synthesis, SnO_2 and S powder precursors were located at the center and upstream of the tube furnace, respectively. SiO_2 substrates were placed close to each other at downstream of the tube furnace. The 2D crystals were obtained on the SiO_2 substrates by heating the tube furnace to 705 °C and maintaining this temperature for 40 min before cooling down to room temperature (RT) (see Section 4 for details).

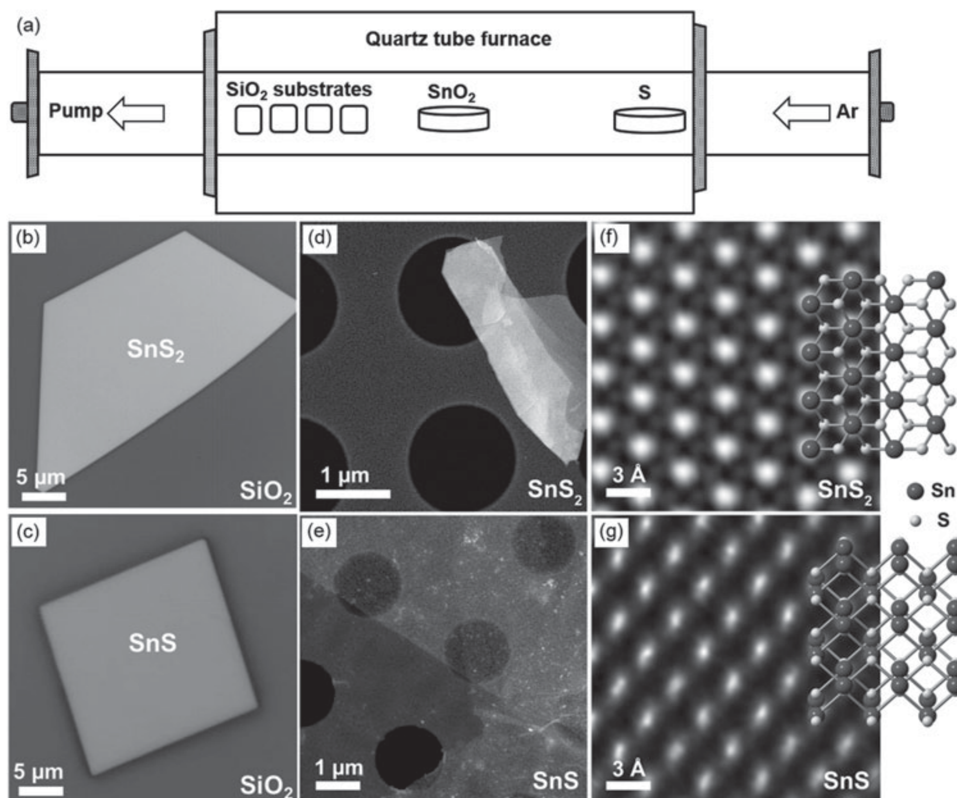

Figure 1. a) The growth setup for the growth of SnS_2 and SnS crystals. Optical microscopy images of b) SnS_2 and c) SnS crystals grown on SiO_2 substrates. Low magnification ADF–STEM images of d) SnS_2 and e) SnS crystals transferred to a TEM grid. Filtered atomic-resolution ADF–STEM image of f) SnS_2 and g) SnS. Ball-and-stick models are overlapped to highlight atomic positions.

© 2016 Wiley-VCH Verlag GmbH & Co. KGaA, Weinheim

Optical images of the SiO_2 substrates show that SnS_2 crystals (Figure 1b) grow at a lower substrate temperature of ≈425 °C while SnS crystals (Figure 1c) form at a higher temperature of ≈550 °C. SnS_2 crystals show a trapezoidal shape, and SnS crystals have a rectangular shape.

Since SnS and SnS_2 possess different crystal structures, atomic resolution STEM imaging can be used to directly verify the phases obtained from the growth. SnS_2 and SnS crystals obtained by the previously described recipe were first transferred to separate TEM grids and imaged in a STEM (see Section 4 for details). Figure 1d,e show low magnification annular dark-field (ADF)–STEM images of SnS_2 and SnS crystals, respectively. Figure 1f,g show filtered high-resolution ADF–STEM images of both phases obtained along the [001] zone axis where the crystal structure of the two phases can be distinguished. The image filtering procedure followed that used by Wu et al.[30] SnS_2, as seen in the ADF–STEM image, appears to crystallize in the 1T polymorph. This arrangement is similar to that observed for 1T-MoS_2.[31,32] On the other hand, the ADF–STEM image of SnS shows its orthorhombic arrangement, which can be clearly differentiated from the image of SnS_2.

2.2. Growth Mechanisms

The growth of the 2D crystals can be explained by the reaction of SnO_2 and S. When the temperature of the tube furnace is above the Tammann temperature of SnO_2 (T_{Tam} = ≈400 °C[33]), SnO_2 evaporation will be initiated, even though the applied temperature is lower than its melting point in powder form (T_{melt} ≈ 1350 °C[34]). At the early stage of the growth (≈400 °C), SnO_2 vapor from solid SnO_2 powders makes contact with the substrate and forms small SnO_2 clusters which act as nucleation sites for tin sulfide crystals.[35]

SnO_2 vapor from solid SnO_2 powders reacts with S vapor to initiate the formation of SnS_2 according to (1)[3]

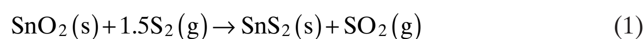

$$\mathrm{SnO_2\,(s) + 1.5S_2\,(g) \rightarrow SnS_2\,(s) + SO_2\,(g)} \quad (1)$$

As the reaction temperature increases, the growth of SnS_2 will eventually stop due to its phase instability on the high temperature.[2,36,37] At the same time, S source will be eventually depleted, which results in a reducing atmosphere in the tube. As a result, SnS growth will be favored according to (2)[3]

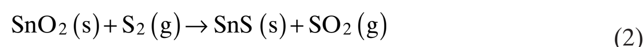

$$\mathrm{SnO_2\,(s) + S_2\,(g) \rightarrow SnS\,(s) + SO_2\,(g)} \quad (2)$$

To help further understand the underlying growth mechanisms of tin sulfide crystals, we performed a series of experiments by using three different growth recipes. Recipe I served as the control experiment where the furnace with the quartz tube was heated from RT to 705 °C and then kept at this temperature for 40 min, followed by cooling down to RT. In recipe II, the furnace with the quartz tube was heated from RT to 625 °C, and immediately cooled down to RT without further heating. For recipe III, the quartz tube was initially held outside the furnace. While the furnace was being heated to 705 °C, the quartz tube was immediately slid inside the furnace at 625 °C. Then, the furnace with the quartz tube was kept at 705 °C for 40 min, followed by cooling down to RT. Only one long rectangular SiO_2 substrate was used for each experiment, and the growth parameters such as heating rate, gas flow rate, pressure, precursors, and substrates were kept constant for all the experiments.

Recipe I yielded both SnS_2 and SnS crystals, but the two were spatially separated on the substrate as shown in **Figure 2**a. SEM imaging (Figure 2b,c) and Raman spectroscopy (see Section 2.3) confirmed that SnS was grown on the hotter side of the substrate compared to SnS_2. On the other hand, recipe II resulted in primarily SnS_2 crystals at the lower temperature side of the substrate while recipe III gave mainly SnS crystals, which appears only in the hotter region. These results indicate that the growth of SnS_2 crystals is initiated mostly during the early stage of heating, while the formation of SnS crystals starts in the later stage of the heating. Hence, the formation of SnS occurs at higher temperatures compared to that of SnS_2, which is consistent with results of previous reports on the growth of SnS_2 and SnS crystals.[2,36,37]

We also studied the trace reaction products of SnO_2 (Figure 2d) and S found in the SnO_2 crucible. It was found that recipe II produced yellow transparent SnS_2 powders (Figure 2e), while recipes I and II yielded dark grey SnS powders (Figure 2f) as confirmed by Raman spectroscopy (see Section 2.3). For recipe II, since the growth was performed at low temperature for a short period of time, SnO_2 powders was sulfurized to form solid SnS_2 as a result of the reaction according to Equation (1). For recipes I and III, as the reaction proceeds, solid SnS_2 dissociation occurs as a result of the incongruent sublimation, which is promoted by both high temperature and S depletion.[38] The dissociation of solid SnS_2 results in the phase transition from SnS_2 to SnS by (3)[38]

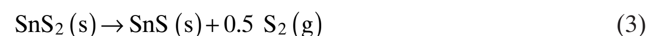

$$\mathrm{SnS_2\,(s) \rightarrow SnS\,(s) + 0.5\ S_2\,(g)} \quad (3)$$

In this series of experiments, we also observed a growth of multi-stacked SnS_2 crystals (Figure 2g–i). The interlayer S vdW interactions between consecutive SnS_2 layers can result in misorientation of the layers during growth. 2D multi-stacked SnS_2 crystals with varying configurations may possess some novel electronic and optical properties. Controlling stacking is beyond our scope in this study, but we point out that this simple method can be further optimized in order to achieve the control over the stacking.

2.3. Raman Spectra and Calculated Vibrational Frequencies

We performed Raman spectroscopy on the SnS_2 and SnS crystals obtained by the discussed growth recipes. The Raman spectra of an 8L SnS_2 crystal (≈5.08 nm as measured in AFM with monolayer thickness of 0.6 nm[1]) show a strong Raman peak at 314.9 cm^{-1}, corresponding to the A_{1g} phonon mode[39] of SnS_2 (**Figure 3**a–c). In addition to the A_{1g} mode, an intra-layer E_g mode[39] with peak at ≈206.2 cm^{-1} is observed in multilayer (ML) SnS_2 crystal with a thickness of ≈17.94 nm (30L) (Figure 3d–f). The absence of the

© 2016 Wiley-VCH Verlag GmbH & Co. KGaA, Weinheim

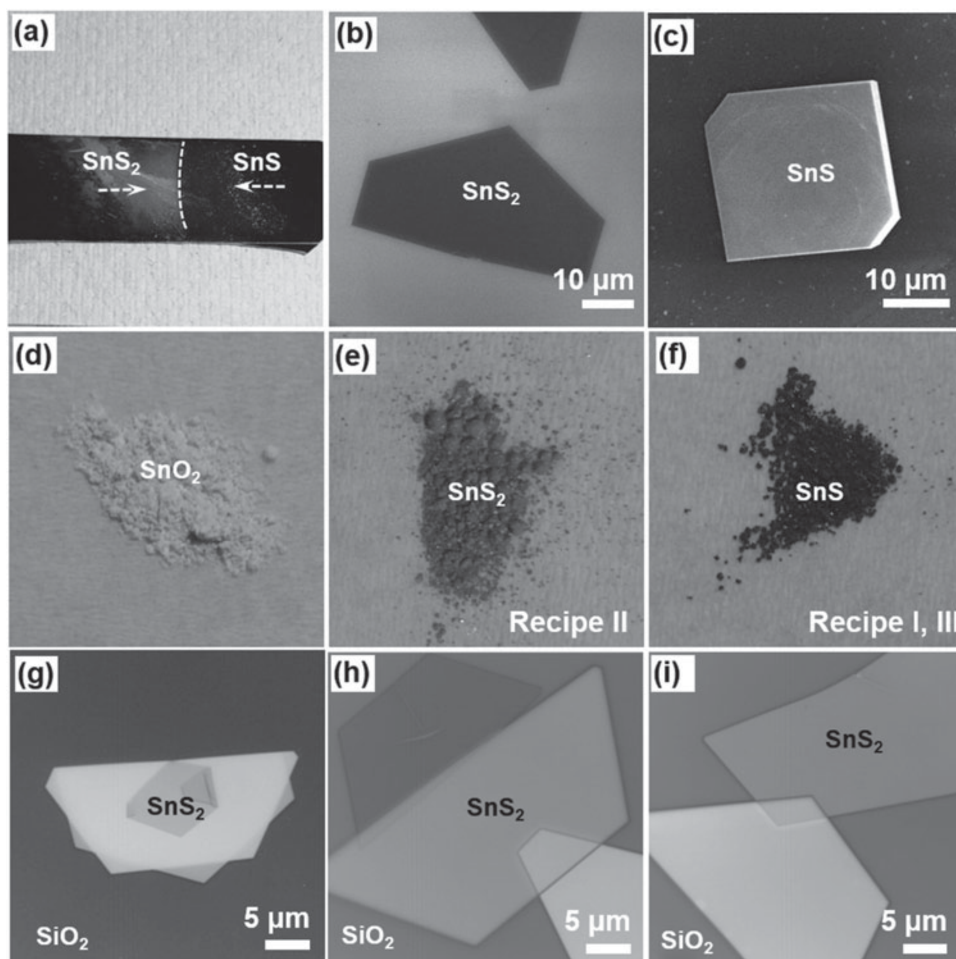

Figure 2. a) Photo image of a long SiO_2 substrate after the growth. A stark boundary on the substrate surface of 2D SnS crystals in the high-temperature region of the tube furnace to 2D SnS_2 crystals in the cooler region can be seen. SEM images of an b) SnS_2 crystal and an c) SnS crystal obtained from the surface of the SiO_2 substrate in (a). Photo images of d) SnO_2 powders, e) SnS_2 powders obtained by recipe II, and f) SnS powders obtained by recipes I and III. g–i) Optical images of multi-stacked SnS_2 crystals.

E_g mode in the 8L SnS_2 is presumably due to the undetectably weak rejection of the Rayleigh scattered radiation.[8] The Raman spectra from a ML SnS crystal (Figure 3g) was also measured. The thickness of the SnS crystal was estimated to approximately 30L (determined by cross-sectional STEM image in Figure 3h). The Raman spectra of the SnS crystal show a very different Raman pattern (Figure 3i) with the peaks centered within the range of 50–250 cm^{-1}. The peaks at 95.6, 192.0, and 218.3 cm^{-1} can be assigned to the A_g mode, and the peak at 163.9 cm^{-1} corresponds to the B_{3g} phonon mode[3,40] of SnS.

To support results of the experimental Raman spectroscopy, we calculated the zone-center vibrational modes of bulk SnS_2 and SnS using ab initio DFT (see Section 4 for details). The vibrational modes at Γ point gave us insight into the allowed Raman active modes for each phase. For bulk SnS_2, we calculated the vibrational modes that correspond to the out-of-plane A_{1g} and in-plane E_g Raman active modes. The calculated values of 313 and 204 cm^{-1} obtained for the A_{1g} and E_g modes, respectively, are in good agreement with the Raman spectrum we obtained for the 2D SnS_2 crystal (**Table 1**).

For bulk SnS, we also calculated vibrational modes that correspond to the A_g and B_{3g} Raman active modes of the bulk orthorhombic structure of SnS. Based on the displacements of these modes, we determined A_g modes at 95, 196, and 216 cm^{-1} and the B_{3g} mode at 163 cm^{-1}. These values are also in good agreement with our assignment of the Raman modes using the measured Raman spectra (Table 1) and prior Raman scattering studies on SnS.[40]

The agreement between our theoretical calculations of the Raman modes for each phase of tin sulfides and our experimental Raman spectra is further demonstration of the controlled growth we have over each phase. Moreover, we do not observe Raman peaks at 474, 632, or 774 cm^{-1} associated with SnO_2.[41] This implies negligible chemical reaction between the crystals and substrate.[35]

2.4. Electronic Structure: Experiment and Calculation

The ionization potential for each tin sulfide phase can be determined by UPS. Using the helium (He) source at photon energies of 21.22 eV, we determined the ionization

© 2016 Wiley-VCH Verlag GmbH & Co. KGaA, Weinheim

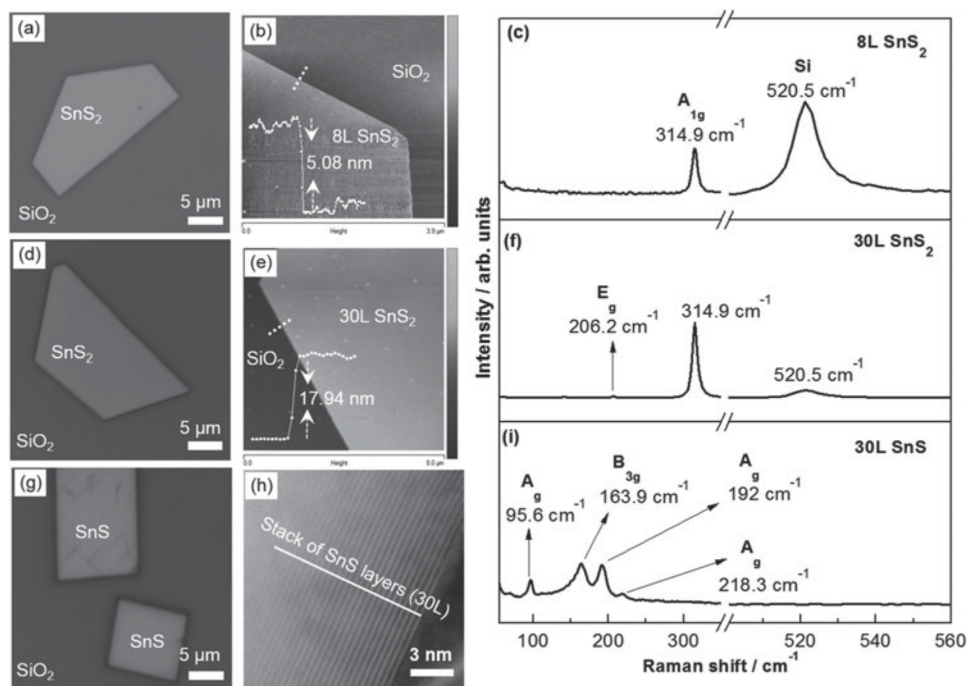

Figure 3. Optical image, AFM image and Raman spectra of a–c) an 8L SnS_2 crystal and d–f) a 30L SnS_2 crystal. g–i) Optical image, cross-sectional ADF–STEM image and Raman spectra of a ≈30L SnS crystal.

potential, ϕ, by subtracting the width of the UPS spectra from 21.22 eV. We determined the ionization potential of our as grown SnS_2 and SnS crystals and compared them to the measurements on commercial SnS_2 crystals (2Dsemiconductors Inc.). The ionization potential of our as-grown SnS_2 was found to be 7.51 eV (**Figure 4**a), close to that of commercial SnS_2 crystal (7.7 eV) (Figure 4b). The ionization potential of SnS was determined to be 5.78 eV (Figure 4c).

Using DFT we evaluated the ionization potentials for SnS and SnS_2 using an explicit slab model. 8L slabs of (001) SnS_2 and (100) SnS were predicted to have bandgaps of 2.31 and 1.07 eV, respectively, which are close to the bandgap values for the respective bulk structures. Calculations of each 8L structure were then used to obtain the difference between the average of the electrostatic potential in the bulk and the eigenenergies with respect to the vacuum potential. This provided an ionization potential of 7.51 and 4.9 eV for SnS_2 and SnS, respectvely, which is in good agreement with the ionization potential of 7.51 and 5.78 eV we obtain for SnS_2 and SnS, respectively.

3. Conclusion

Highly crystalline 2D SnS_2 and SnS crystals with lateral sizes over tens of microns have been directly synthesized on SiO_2

Table 1. Comparison of experimentally measured and ab initio DFT calculated Raman spectra peak positions in SnS_2 and SnS in cm^{-1}.

Phases	SnS_2		SnS			
Raman modes	A_{1g}	E_g	A_g	A_g	A_g	B_{3g}
Experimental	314.9	206.2	95.6	192	218.3	163.9
Calculated	313	204	95	196	216	163

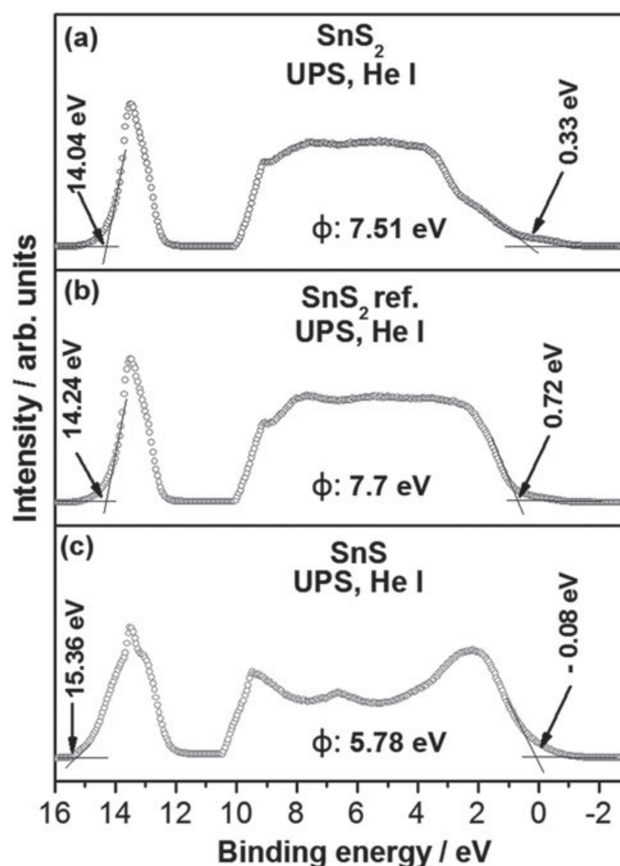

Figure 4. UPS spectra acquired for a) our as-grown SnS_2, b) commercial SnS_2 crystal, and c) our as-grown SnS crystal.

© 2016 Wiley-VCH Verlag GmbH & Co. KGaA, Weinheim

substrates using a simple atmospheric pressure vapor-phase method. High-resolution ADF–STEM imaging reveals the phases of 2D hexagonal SnS_2 (1T) and orthorhombic SnS crystals. The phase purity of SnS_2 and SnS crystals is confirmed by the analysis of the Raman and UPS spectra, and the results are corroborated by ab initio DFT calculations. A series of growth experiments are performed to determine the growth process of the 2D crystals. It is found that temperature determines the phase of each crystal. SnS_2 crystals grow at lower temperatures compare to the case of SnS crystals. Moreover, we have showed that the hexagonal SnS_2 phase can be transformed into orthorhombic SnS phase upon high temperature treatment during growth. This temperature controlled process is advantageous for the purpose of avoiding highly toxic byproducts such as H_2S in H_2 reduction. Overall, these results are useful for future studies of the structural, electronic, and optical properties of 2D hexagonal SnS_2 and orthorhombic SnS and may offer important guidance for realizing SnS_2- and SnS-based electronic and optoelectronic devices.

4. Experimental Section

Materials Growth: SnO_2 and S powders were used as source materials in a conventional single-zone horizontal quartz tube (1 in.) furnace. In a typical experiment, SnO_2 (≈15 mg) powders in a quartz crucible were placed in the center of the tube furnace. Also, S (≈350 mg) powders in a quartz crucible were placed 13 cm upstream from the center of the tube furnace. The degenerately boron-doped (0.001–0.005 Ω cm) silicon (Si) substrates (≈1 × 1 cm^2) with 285 nm SiO_2 capping layer were cleaned by sonication in acetone and isopropyl alcohol (IPA) baths, sequentially for ≈1 min each, followed by drying with a nitrogen (N_2) gas. The SiO_2 substrates were placed downstream to the center at a distance of about 9 (where the temperature was ≈550 °C) and 11.5 cm (where the temperature was ≈425 °C), respectively, for the growth of SnS and SnS_2 crystals, respectively. The temperature of the substrates was determined by using a type K thermocouple. The tube furnace was pumped down to remove the air and then filled with a high-purity argon (Ar) gas (≈100 sccm) to atmospheric pressure. The center of heating zone was heated to 705 °C within 35 min. When the center of heating zone reached 705 °C, the temperature of the S powders was measured to be ≈350 °C by using the thermocouple. The tube furnace was kept at 705 °C for 40 min, and cooled down to RT.

STEM Sample Preparation and Characterization: To transfer the as-grown crystals from a SiO_2 substrate to a Cu TEM grid, an all-dry transfer method that employs a polydimethylsiloxane (PDMS) film (Gel-Pak PF-20-X4) was developed. Briefly, the PDMS film was placed on the as-grown crystals on the SiO_2 substrate and then peeled off. To ensure the transfer of the crystals from the SiO_2 substrate to the PDMS film, the film was slightly rubbed on by a q-tip. Next, the TEM grid was placed on the area of the film and then peeled off. FEI Titan G2 60–300 aberration-corrected STEM equipped with a CEOS DCOR probe corrector was used in this study. ADF–STEM images (2048 × 2048 $pixel^2$) were acquired with the STEM operated at 200 keV using a dwell time of 6 µs per image pixel at a camera length of 130 mm. The beam convergence angle, α_{obj}, was measured to be 26 mrad. The ADF detector inner and outer angles of collection were measured to be 54 and 317 mrad, respectively. The measured probe size was ≈0.8 Å.

UPS Characterization: UPS characterization was carried out by using a Kratos AXIS ULTRADLD XPS system equipped with a He I of UV source. The aperture for UPS has a diameter of 110 µm. Vacuum pressure was kept below 3×10^{-9} torr, and neutralizer was applied during the data acquisition. For UPS spectra comparison, commercial available bulk SnS_2 crystals (2Dsemiconductors Inc.) were used.

Additional Characterizations: Microstructural analyses were done by a FEI NNS450 SEM. Optical microscopy analyses were performed with a Nikon Y-FL optical microscope. Raman spectra were collected using a Horiba system with a 532 nm laser (<2 mW excitation power, 100× objective lens). For Raman spectra comparison purposes, commercial available bulk SnS_2 crystals (2Dsemiconductors Inc.) were used. All Raman spectra were calibrated using the 520.5 cm^{-1} line of a Si wafer. Thickness measurements were performed using Veeco Dimension 5000 AFM in tapping mode.

Calculations: The calculations were based on the first-principles DFT and density functional perturbation theory using the projector augment wave method as implemented in the software package VASP.[42] For the electronic structure calculations, a Monkhorst–Pack scheme was adopted to integrate over the Brillouin zone with a k-mesh of 12 × 12 × 8 (8 × 8 × 1) for the bulk (few-layer) structures. A plane-wave basis kinetic energy cutoff of 500 eV was used. vdW interactions in bulk and few-layer SnS_2 were accounted for using a semi-empirical correction to the Kohn Sham energies when optimizing each structure.[43] The optimized lattice constants for bulk SnS_2 and SnS were a = 3.70 Å, c = 11.85 Å and a = 4.35 Å, b = 3.99 Å and c = 11.21 Å, respectively. This study used the Heyd–Scuseria–Ernzerhof (HSE) hybrid functional to obtain accurate values for the bandgaps and ionization potentials for each phase.[44] The HSE calculations incorporated 25% short-range Hartree–Fock exchange and the screening parameter was set to 0.2 $Å^{-1}$. Calculations of the vibrational frequencies at Γ point relied on density functional perturbation theory.

Acknowledgements

Financial support for this work was provided by two STARnet centers, C-SPIN and FAME, through the SRC sponsored by MARCO and DARPA. This work used XSEDE (NSF, ACI-1053575) and UPS instrumentation (NSF, DMR-0958796). STEM analysis was performed in the Characterization Facility of the University of Minnesota, which receives partial support from NSF through the MRSEC program (DMR-1420013).

[1] Y. Huang, E. Sutter, J. T. Sadowski, M. Cotlet, O. L. A. Monti, D. A. Racke, M. R. Neupane, D. Wickramaratne, R. K. Lake, B. A. Parkinson, P. Sutter, *ACS Nano* **2014**, *8*, 10743.
[2] L. A. Burton, D. Colombara, R. D. Abellon, F. C. Grozema, L. M. Peter, T. J. Savenije, G. Dennler, A. Walsh, *Chem. Mater.* **2013**, *25*, 4908.
[3] J.-H. Ahn, M.-J. Lee, H. Heo, J. H. Sung, K. Kim, H. Hwang, M.-H. Jo, *Nano Lett.* **2015**, *15*, 3703.

© 2016 Wiley-VCH Verlag GmbH & Co. KGaA, Weinheim

[4] X. Hu, G. Song, W. Li, Y. Peng, L. Jiang, Y. Xue, Q. Liu, Z. Chen, J. Hu, *Mater. Res. Bull.* **2013**, *48*, 2325.
[5] S. K. Panda, A. Antonakos, E. Liarokapis, S. Bhattacharya, S. Chaudhuri, *Mater. Res. Bull.* **2007**, *42*, 576.
[6] N. G. Deshpande, A. A. Sagade, Y. G. Gudage, C. D. Lokhande, R. Sharma, *J. Alloys Compd.* **2007**, *436*, 421.
[7] Á. Szabó, S. J. Koester, M. Luisier, *IEEE Electron Device Lett.* **2015**, *36*, 514.
[8] H. S. Song, S. L. Li, L. Gao, Y. Xu, K. Ueno, J. Tang, Y. B. Cheng, K. Tsukagoshi, *Nanoscale* **2013**, *5*, 9666.
[9] G. Su, V. G. Hadjiev, P. E. Loya, J. Zhang, S. Lei, S. Maharjan, P. Dong, P. M. Ajayan, J. Lou, H. Peng, *Nano Lett.* **2015**, *15*, 506.
[10] J. W. Seo, J. T. Jang, S. W. Park, C. Kim, B. Park, J. Cheon, *Adv. Mater.* **2008**, *20*, 4269.
[11] R. Schlaf, O. Lang, C. Pettenkofer, W. Jaegermann, *J. Appl. Phys.* **1999**, *85*, 2732.
[12] K. Chang, Z. Wang, G. Huang, H. Li, W. Chen, J. Y. Lee, *J. Power Sources* **2012**, *201*, 259.
[13] S. S. Hegde, A. G. Kunjomana, K. A. Chandrasekharan, K. Ramesh, M. Prashantha, *Phys. B Condens. Matter* **2011**, *406*, 1143.
[14] A. Tanusevski, *Sol. Energy Mater. Sol. Cells* **2003**, *80*, 297.
[15] W. Wang, K. K. Leung, W. K. Fong, S. F. Wang, Y. Y. Hui, S. P. Lau, Z. Chen, L. J. Shi, C. B. Cao, C. Surya, *J. Appl. Phys.* **2012**, *111*, 093520.
[16] N. Koteswara Reddy, K. Ramakrishna Reddy, *Thin Solid Films* **1998**, *325*, 4.
[17] G. A. Tritsaris, B. D. Malone, E. Kaxiras, *J. Appl. Phys.* **2013**, *113*, 233507.
[18] R. Guo, X. Wang, Y. Kuang, B. Huang, *Phys. Rev. B* **2015**, *92*, 115401.
[19] M. Ristov, G. Sinadinovski, I. Grozdanov, M. Mitreski, *Thin Solid Films* **1989**, *173*, 53.
[20] P. Sinsermsuksakul, J. Heo, W. Noh, A. S. Hock, R. G. Gordon, *Adv. Energy Mater.* **2011**, *1*, 1116.
[21] Z. Deng, D. Cao, J. He, S. Lin, S. M. Lindsay, Y. Liu, *ACS Nano* **2012**, *6*, 6197.
[22] T. Sorgenfrei, F. Hofherr, T. Jauß, A. Cröll, *Cryst. Res. Technol.* **2013**, *48*, 193.
[23] M. M. Nassary, *J. Alloys Compd.* **2005**, *398*, 21.
[24] M. Cruz, J. Morales, J. P. Espinos, J. Sanz, *J. Solid State Chem.* **2003**, *175*, 359.
[25] Z. Mutlu, M. Ozkan, C. S. Ozkan, *Proc. SPIE* **2015**, *9552*, doi: 10.1117/12.2190598.
[26] Z. Mutlu, S. Shahrezaei, S. Temiz, M. Ozkan, C. S. Ozkan, *J. Electron. Mater*, *45*, 2115.
[27] B. Ghosh, M. Das, P. Banerjee, S. Das, *Appl. Surf. Sci.* **2008**, *254*, 6436.
[28] J. Xia, D. Zhu, L. Wang, B. Huang, X. Huang, X.-M. Meng, *Adv. Funct. Mater.* **2015**, *25*, 4255.
[29] J. Xia, X.-Z. Li, X. Huang, N. Mao, D.-D. Zhu, L. Wang, H. Xu, X. Meng, *Nanoscale* **2016**, *8*, 2063.
[30] R. J. Wu, M. Topsakal, T. Low, M. C. Robbins, N. Haratipour, J. S. Jeong, R. M. Wentzcovitch, S. J. Koester, K. A. Mkhoyan, *J. Vac. Sci. Technol. A.* **2015**, *33*, 060604.
[31] R. J. Wu, M. L. Odlyzko, K. A. Mkhoyan, *Ultramicroscopy* **2014**, *147*, 8.
[32] G. Eda, H. Yamaguchi, D. Voiry, T. Fujita, M. Chen, M. Chhowalla, *Nano Lett.* **2011**, *11*, 5111.
[33] A. Davidson, B. Morin, M. Che, *Colloid Surf. A* **1993**, *72*, 245.
[34] Z. R. Dai, Z. W. Pan, Z. L. Wang, *J. Am. Chem. Soc.* **2002**, *124*, 8673.
[35] Y.-B. Yang, J. K. Dash, A. J. Littlejohn, Y. Xiang, Y. Wang, J. Shi, L. H. Zhang, K. Kisslinger, T.-M. Lu, G.-C. Wang, *Cryst. Growth Des.* **2016**, *16*, 961.
[36] L. A. Burton, A. Walsh, J. Phys. *J. Phys. Chem. C* **2012**, *116*, 24262.
[37] L. Price, I. Parkin, A. Hardy, R. Clark, *Chem. Mater.* **1999**, *11*, 1792.
[38] T. Zhou, W. K. Pang, C. Zhang, J. Yang, Z. Chen, H. K. Liu, Z. Guo, *ACS Nano* **2014**, *8*, 8323.
[39] J. Xia, D. Zhu, L. Wang, B. Huang, X. Huang, X.-M. Meng, *Adv. Funct. Mater.* **2015**, *25*, 4255.
[40] H. R. Chandrasekhar, R. G. Humphreys, U. Zwick, M. Cardona, *Phys. Rev. B* **1977**, *15*, 2177.
[41] S. H. Sun, G. W. Meng, G. X. Zhang, T. Gao, B. Y. Geng, L. D. Zhang, J. Zuo, *Chem. Phys. Lett.* **2003**, *376*, 103.
[42] G. Kresse, J. Hafner, *Phys. Rev. B* **1993**, *47*, 558.
[43] S. Grimme, *J. Comput. Chem* **2006**, *27*, 1787.
[44] J. Heyd, G. E. Scuseria, M. Ernzerhof, *J. Chem. Phys.* **2003**, *118*, 8207.

Received: February 19, 2016
Revised: March 9, 2016
Published online: April 21, 2016

© 2016 Wiley-VCH Verlag GmbH & Co. KGaA, Weinheim